







# Investigation of Factors Affecting Corrosion Mechanisms in Latent Heat Thermal Energy Storage Systems

Gaurav Vithalani<sup>1\*</sup>, Stuart Bell<sup>1</sup>, Geoffrey Will<sup>2</sup>, Theodore A. Steinberg<sup>1</sup>,  
Richard Clegg<sup>3</sup>, and Rezwanul Haque<sup>2</sup>

<sup>1</sup> Queensland University of Technology, Australia

<sup>2</sup> University of the Sunshine Coast, Australia

<sup>3</sup> Explicom Engineering Investigators, Australia

\*Correspondence: Gaurav Vithalani, [gauravlitbhai.vithalani@hdr.qut.edu.au](mailto:gauravlitbhai.vithalani@hdr.qut.edu.au)

**Abstract.** Concentrated Solar Power (CSP) plants integrated with Latent Heat Thermal Energy Storage (LHTES) systems offer a promising solution for dispatchability, reliability, and economic concerns generally associated with renewable energy technologies. These systems, however, require an operational life of up to 30 years to compete with power plant systems operating on fossil fuels. This is a significant challenge due to the high temperatures and corrosive eutectic salts utilised in LHTES systems. Additionally, these systems and its subcomponents are expected to be under varying degrees of stress due to the diurnal cyclic temperature variations inherent in the plant's operational cycle. Hence, it is crucial to understand the various factors that can affect the operational life of materials used in such applications and conduct thorough material compatibility studies to assess the combined impact of these operating conditions on corrosion mechanisms. This study presents a novel static immersion test approach using modified Compact Tension (CT) specimens manufactured from 316L to investigate the effects of Na<sub>2</sub>CO<sub>3</sub>:NaCl (59.45:40.55 wt.%) salt, elevated temperatures (700 °C for up to 1000 hours), and stress on corrosion induced in the alloy. The post-exposure results are characterised with Scanning Electron Microscopy (SEM) and Energy Dispersive Spectroscopy (EDS) shows that corrosion mechanisms are significantly affected by factors such as high operating temperatures leading to changes in both corrosion morphology and rate, high stresses causing localised preferential corrosion, as well as corrosive salt and oxygen availability affecting the type of corrosion induced.

**Keywords:** Concentrated Solar Power (CSP), Latent Heat Thermal Energy Storage (LHTES), Compact Tension (CT) Specimen, Chloride Carbonate Salt, 316L Corrosion.

## 1. Introduction

The demand for the development of more efficient renewable energy systems has been driving the technological advancement of alternate energy generation and storage methods. To address various dispatchability, reliability and economic concerns, Concentrated Solar Power (CSP) plants integrated with Latent Heat Thermal Energy Storage (LHTES) are a promising alternative to conventional combustion power plants. These CSP plants, however, must operate reliably for up to 30 years to achieve a levelized cost of electricity similar to power plant

systems operating on fossil fuels, which poses a substantial challenge due to the harsh operational conditions of the system.

Next generation CSP plants using LHTES are expected to operate at temperatures up to 800 °C, with LHTES storing heat energy at temperatures up to 750 °C using Phase Change Material (PCM) such as eutectic salts. The stored heat is transferred back to the Heat Transfer Fluid (HTF) to deliver heat for up to 8 hrs [1]. The operational environment substantially affects the type of corrosion induced in any given system, impacting the compatibility of the material to be used in the plant, making it crucial to understand the unique environment of the LHTES system being considered to study the effects of the operational environment on the alloys [2]. Furthermore, the LHTES system will be under varying degrees of stress due to the inherent diurnal cyclic temperature variations in the plant, which could initiate a multitude of failure modes in the metal alloys and detrimentally affect the operational life of the system. While these factors can significantly impact the mode and rate of failure, the combined impact of corrosion and stress is often neglected during the material compatibility and life cycle assessment of CSP systems. Therefore, a more thorough understanding of these factors is crucial to enhance material compatibility assessment for LHTES systems. In addition, this understanding will aid in examining stress assisted corrosion and its underlying mechanisms to develop mitigation strategies leading to improved reliability, sustainability, and safety of critical infrastructure.

## 2. Methodology

A novel static immersion testing approach was utilised with Compact Tension (CT) specimens as depicted in Figure 1, modified from the ASTM standard E1820 – 21 [3] based on the work of Turski [4]. The specimens consisted of 10.2 mm and 25 mm thickness where the increase in thickness is expected to increase the probability of failure by reducing the fracture toughness [5]. The experiments were conducted by plastically deforming CT specimens made from 316L to induce residual tensile stresses in the u-notch region, which are then exposed to a eutectic mixture of chloride-carbonate salt and air at temperatures up to 700 °C for up to 1000 hrs.

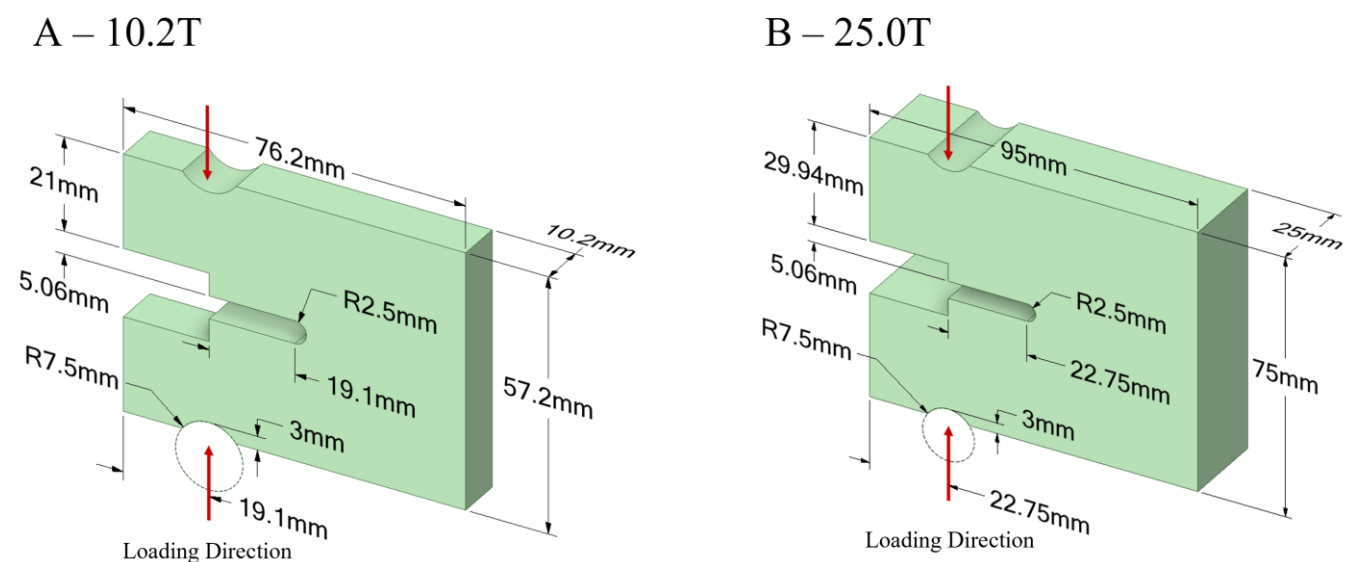


**Figure 1.** CT specimen designs

The experimental parameters utilised to conduct the study, as outlined in Table 1 are selected from published literature [6-9] to aid in understanding the expected interaction of the 316L with its environment for this comparative study.

**Table 1. Experimental Parameters.**

Sample	CT specimen	Environment	Salt Mass	Temperature (°C)	Test time (Hours)
S1	10.2 T	NaCl:Na <sub>2</sub> CO <sub>3</sub>	~ 200 gm	650	500
S2	"	"	"	"	1000
S3	"	Air	---	"	500
S4	"	"	---	"	1000
S5	"	"	---	700	500
S6	"	"	---	"	1000
S7	25 T	NaCl:Na <sub>2</sub> CO <sub>3</sub>	~ 380 gm	650	500

" Same as above

The prestressed samples S1 and S2 were placed in ceramic crucibles of 60 mm Outer Diameter (OD) and 100 mm height, while S7 was placed in a 316L crucible of 80 mm OD and 100 mm height and submerged in salt, whereas S3-S6 were placed directly in the furnace. The crucible sizes were selected to account for the difference in specimen size, resulting in a higher salt quantity required for S7. The experiments were conducted by initiating the tests with 4 hours of a drying cycle at 350°C to remove any potential moisture in the eutectic mixture of salts. Following the drying cycle, the furnace was maintained at a constant peak temperature as required for each experiment until the end of the exposure period. The samples were then extracted from the mid-section of the CT specimen around the u-notch region where the stress concentration is expected based on the Finite Element Analysis (FEA) conducted on a 316L CT specimen. The samples are then polished and mounted on conductive epoxy resin to analyse the effects of thermal aging through Scanning Electron Microscopy (SEM), Energy Dispersive Spectroscopy (EDS), and optical microscopy.

### 3. Results

#### 3.1 Effect of High Temperature

The impact of high temperature on oxidation mechanisms is analysed through samples S3-S6 aged in air at 650 °C (S3, S4) and 700 °C (S5, S6). The maximum thickness of the oxide layer is observed through BSE images and analysed where samples aged at the same temperatures are averaged for simplified observation of any evident difference caused by temperature.

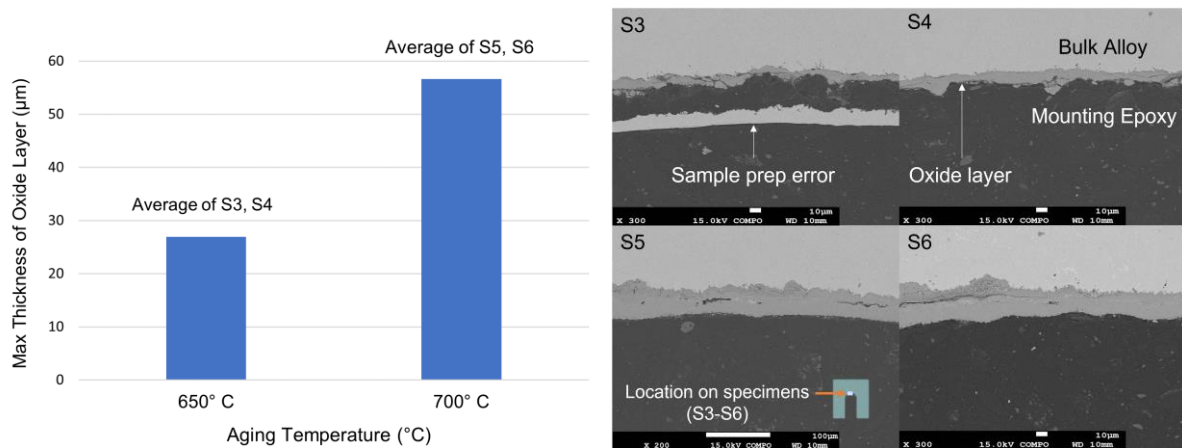


**Figure 2. BSE images and comparison of maximum oxide layer thickness observed in samples S3, S5 aged for 500 hours and S4, S6 aged for 1000 hours in air**

As shown in Figure 2, samples aged at 700 °C display higher peak thickness of the oxide layer compared to 650 °C samples. The findings align with literature where the increase

in temperature has been observed to increase oxidation. However, the mechanisms governing which element is oxidised and the growth of oxide films are often not fully explored. Hence, the oxide layers of samples are further analysed through EDS as shown in Figure 3 to understand how the oxidation mechanisms are affected by temperature.

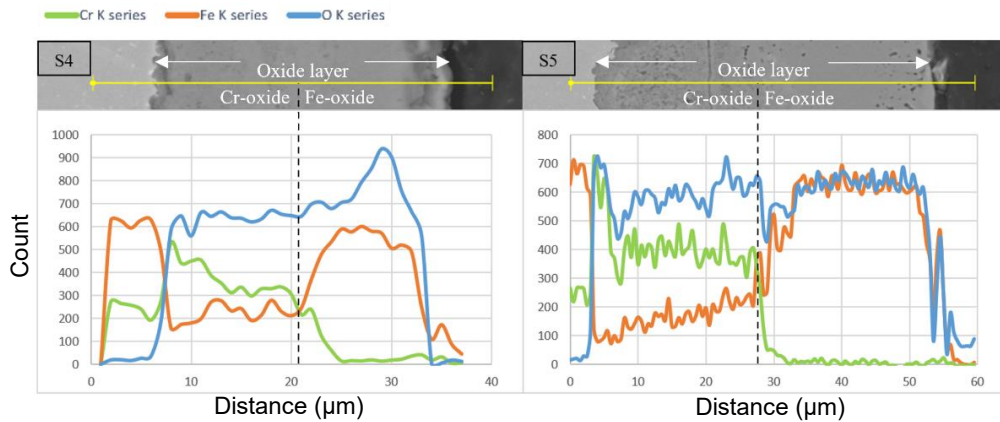


**Figure 3.** Line scan EDS of the oxide layer of S4 aged at 650 °C and S5 aged at 700 °C in air

A set of line scan EDS analyses were performed using an Oxford XMax 80 EDS to identify elements in the oxide layer of the samples. The data presented in Figure 3 shows that both samples S4 and S5 form a binary oxide film consisting of chromium oxide and iron oxide layers. Moreover, it can be observed that the chromium oxide layer in S5 is much more distinguishable compared to S4, considering the higher count of Cr than Fe in the layer. This can be explained by chemical thermodynamics as the Gibbs free energy ( $\Delta G$ ) is a component of temperature, as observed in the Ellingham diagram in Figure 4. It can be observed that Cr-oxides have lower  $\Delta G$  than Fe-oxides, resulting in preferential chromium oxidation; however, the increase in  $\Delta G$  with temperature results in an increased rate of oxidation as observed between Cr-oxides of S5 compared to S4 [10, 11].

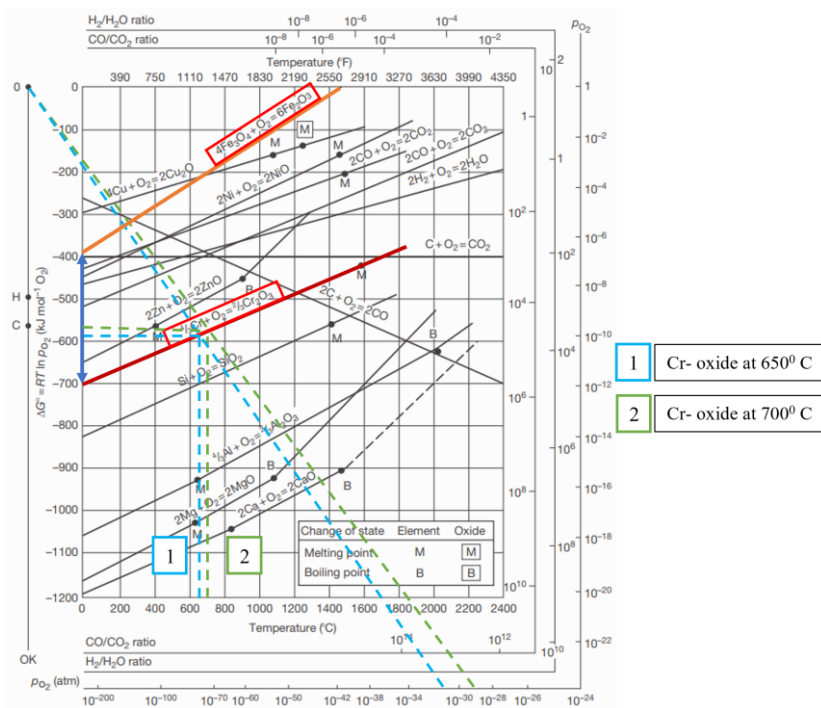


**Figure 4.** Ellingham diagram illustrating  $\Delta G$  as a function of temperature for Cr and Fe oxides (Adapted from [12])

The primary mechanism for the growth of the oxide layer with temperature that can be observed in Figure 2 is oxide kinetics [11]. While the Cr-rich oxides are known to cause passivation, limited oxygen diffusion into the alloy continues through dislocation and grain boundary defects, which increases with temperatures [13]. Moreover, studies have observed temperature dependent increase in porosity in oxides formed on 316 alloys at temperatures above 600° C, allowing inward diffusion of oxygen [14, 15].

### 3.2 Effects of Stress and Chloride-Carbonate Salt

Sample S2 was aged at 650°C in NaCl:Na<sub>2</sub>CO<sub>3</sub> consisting of 59.45:40.55 wt.% eutectic mixture of the salts. The S2 exhibits severe localised corrosion along the salt/metal interface in the high stress region of the sample, as observed in the stitched image in Figure 5.

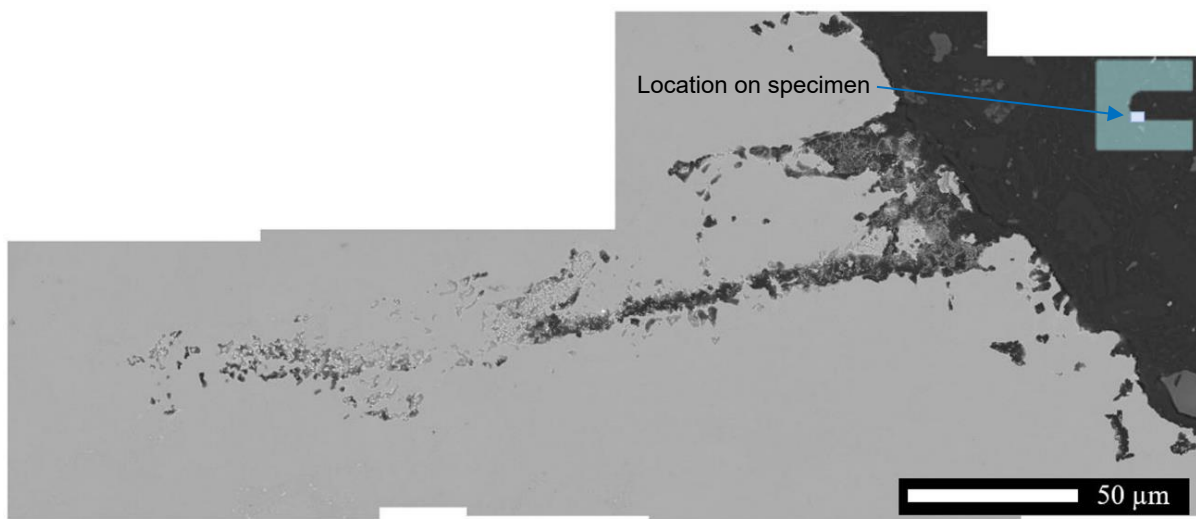


**Figure 5.** Stitched BSE image of defect observed in high stress region of sample S2 after exposure in chloride-carbonate salt at 650°C for 1000 hours

The image stitching method is used as it allows examination of a larger area with high resolution images to observe the defect on the sample with a length of about 245 µm and a width of 61 µm. The defect is localised and does not occur in other regions on the salt/metal interface. Moreover, the discontinuity between the front and end of the defect suggests that it extends across the thickness of the sample. The form of the defect shows similarities to localised corrosion effects such as pitting, crevice or vertical grain attack [16]; however, no instances of such corrosion are found in the published literature for the given environment. Hence, it is further analysed in an attempt to classify the defect and understand the mechanisms involved. First, Secondary Electron (SE) images in the region are acquired using Joel 7001f SEM and analysed to confirm that the defect is within the sample and not debris on the sample surface. Next, EDS maps in the region are required as shown in Figure 6, to observe the effects of the defect on the alloying elements of the 316L sample.

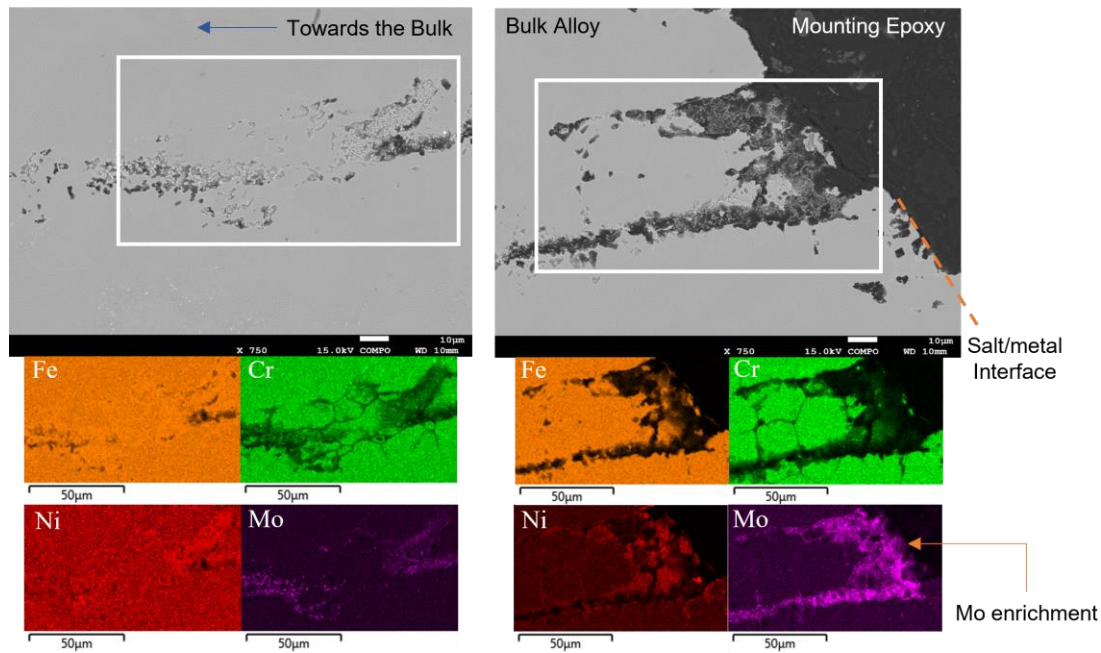


**Figure 6.** Defect observed using BSE images with EDS maps acquired in the region denoted by the white boxes for sample S2 aged in chloride-carbonate salt at 650 °C for 1000 hours

The EDS results in Figure 6 indicates that the Fe-Cr-Ni alloy 316L exhibits dealloying of all of the major alloying elements. However, chromium appears to have been more aggressively dissolved through selective leaching along the defect's length on intergranular and transgranular paths, whereas iron and nickel only appear to have de-alloyed near the salt metal interface. Similarly, molybdenum enrichment is evident at the front of the defect near the interface, whereas the effects are not as prominent going towards the bulk material.

The severity of chromium depletion in the defect is expected as the defect is located in the u-notch region, where the tensile residual stresses are induced after prestressing. The mechanism works through stress assisted diffusion of Cr at the grain boundaries, much faster than in compressive or low stress regions [17, 18]. The retention of iron and nickel towards the end of the defect is attributed to the preferential dissolution of chromium over iron and nickel. Moreover, Cr in Fe-Cr-Ni alloy is responsible for passivity and produces oxides that protect the alloy from dissolution. Alloys under high temperatures and oxidising/corroding environment over a substantial period leads to the dissolution of the passive film, resulting in a rapid increase in corrosion. The location of the film breakdown provides a favourable environment for localised corrosion [19]. Henderson [20] observed Mo enrichment during transpassivation potential in Ni alloys and suggested its significant impact on repassivation following defects such as crevice corrosion. The defect observed could be a form of pitting corrosion, such as a vertical grain attack [21], considering the combined impact of free energy and transpassivation. The location of the defect indicates some role of stress in the formation of the defect in 316L alloy. Moreover, S2, aged for 1000 hours, formed the defect, whereas S1 and S7, aged for 500 hours in the same salt environment and temperature, did not show similar results, suggesting an impact of exposure time along with stress.

### 3.3 Effects of Oxygen Availability

Samples S1 and S7 were aged in the same environment (same temperature and exposure time). However, the post experimental results show a drastic difference in corrosion mechanisms, as evident in Figure 7. The BSE images for samples show an oxide layer and Inter-Granular Corrosion (IGC) with a combined penetration depth of over 300 µm in S7 compared to the dealloying depth of around 25 µm in S1.

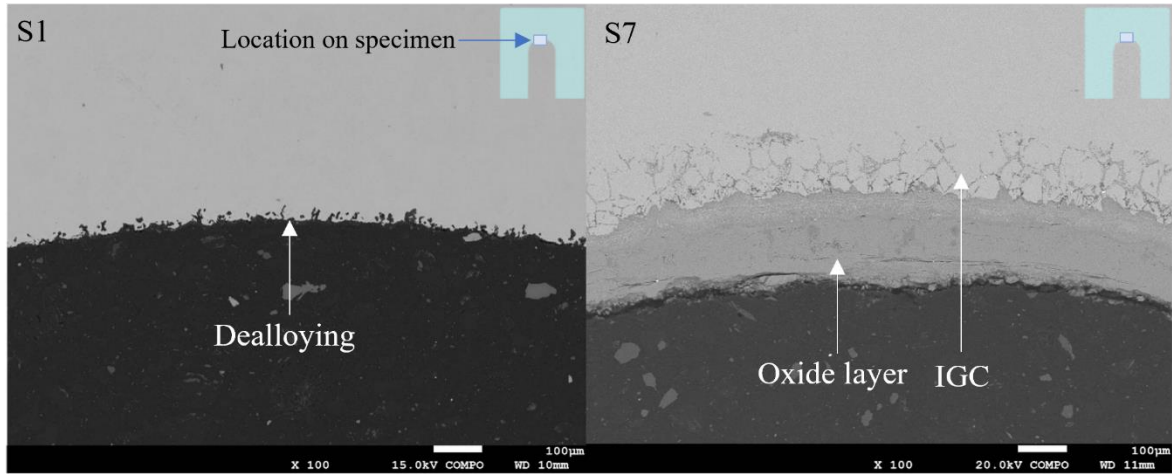


**Figure 7.** Difference in corrosion mechanisms in S1 and S7 manufactured from AISI 316L aged in chloride-carbonate salt at 650 °C for 500 hrs

The sample S1 is 10.2 mm thick, whereas the S7 is a 25 mm thick CT specimen, although that cannot account for the change in corrosion mechanism. However, the materials were ordered from different suppliers to manufacture S1 and S7, which could be a potential cause. The amount of each element in an alloy defines its designation, but each of these elements can exist within an acceptable range in the alloy. For example, 316L alloy could consist of Ni content of 10 to 12%. It is expected that alloy properties would not be significantly impacted by a change of alloying element within this range. Hence, compositions for both the samples are evaluated using portable X-Ray Fluorescence (pXRF) to analyse any potential difference in alloying elements.

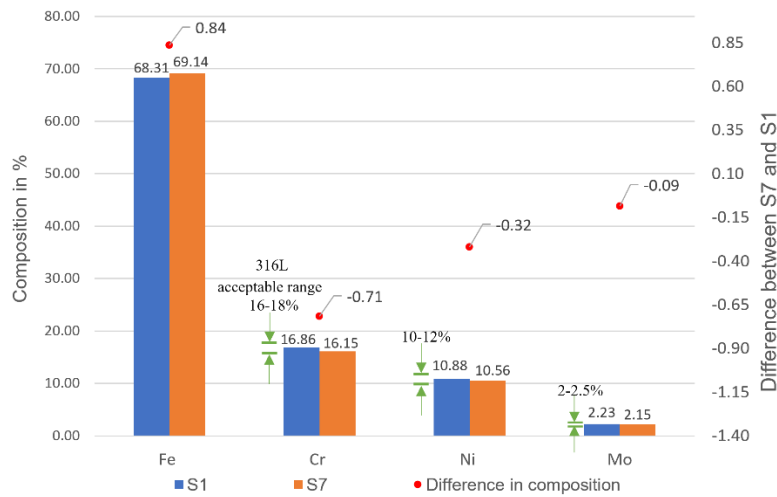


**Figure 8.** Difference in alloy compositions between S1 and S7

The S7 and S1 material compositions were analysed through pXRF with a beam dwell time of 60 seconds. The results indicate that both the samples are within the acceptable range of alloying elements to be classified as 316L. Although, the material compositions in wt.% are slightly different between the samples, as shown in Figure 8. While the content of Fe is slightly higher by 0.84 in S7 compared to S1, the elements generally responsible for corrosion resistance at high temperatures, such as Ni, Cr, and Mo [22], are comparatively lower in S7. However, It is generally assumed that such small changes in the composition do not significantly impact the material properties. This leaves the only remaining variable of oxygen availability in the experiment to offer a possible justification for the material behaviour.

Sample S1 (10.2T) was placed in a crucible with a 60 mm OD and 100 mm height, whereas S7 (25T) was placed in a crucible with 80 mm OD and 100mm to compensate for the difference in the size of the CT specimens. This, in turn, required a higher quantity of salt mass to submerge the S7 specimen compared to S1. However, the reduction in the volume of salt after phase change possibly resulted in the exposure of the S7 to higher amounts of atmospheric air, causing the formation of a multiphase oxide layer and IGC as opposed to the dealloying observed on the S1, which was fully submerged in salt reducing its oxidation potential. This effect can be confirmed by observing sample S2 (10.2T) aged in the same environment exhibiting a similar corrosion mechanism of dealloying as S1.

## 4. Conclusion

The study shows that corrosion mechanisms in 316L are significantly affected by several factors, such as high temperatures, tensile stresses, corrosive salt, and oxygen availability. Combination of these factors can drastically increase the effects of corrosion on alloys, with key results discussed below,

- The combined effect of stress and chloride-carbonate salt was observed through Backscattered Electron (BSE) imaging, which shows severe preferential corrosion with a length of about 245  $\mu\text{m}$  and a width of 61  $\mu\text{m}$  in the high stress region of the sample near the surface in contact with the salts (i.e., salt-metal interface).
- The effect of increase in temperature was observed on samples where an increase in the thickness of the oxide layer was observed on samples aged at 700  $^{\circ}\text{C}$  relative to 650  $^{\circ}\text{C}$ . The combined effect of chemical thermodynamics and oxide kinematics are identified as the mechanisms responsible for this phenomenon.
- The sample submerged in varying amounts of chloride-carbonate salt exhibits drastically different failure modes and corrosion rates caused due to oxygen availability near the salt metal interface. The results show the occurrence of dealloying up to the depth of 25  $\mu\text{m}$  on sample S1, which was fully submerged in salt. However, sample S7, exposed to more oxygen, shows multiphase oxide layer formation and Intergranular Corrosion (IGC) with a combined penetration depth of over 300  $\mu\text{m}$ .

## Data availability statement

Data utilised to acquire the results in this study will be made available upon reasonable request.

## Author contributions

**Gaurav Vithalani:** Conceptualisation, Methodology, Investigation, Resources, Formal analysis, Data Curation, Writing - Original Draft, Writing - Review & Editing. **Stuart Bell:** Conceptualization, Methodology, Investigation, Resources, Supervision, Writing - Review & Editing. **Geoffrey Will:** Conceptualisation, Methodology, Resources, Supervision, Funding acquisition, Writing - Review & Editing. **Theodore Steinberg:** Supervision, Funding acquisition, Writing - Review & Editing. **Richard Clegg:** Conceptualization, Supervision, Writing - Review & Editing. **Rezwatul Haque:** Supervision, Writing - Review & Editing

## Competing interests

The authors declare that they have no known competing financial interests or personal relationships that could have appeared to influence the work reported in this paper.



## Acknowledgement

This work was funded by the Australian Solar Thermal Research Initiative (ASTRI), which is supported by the Australian Government via the Australian Renewable Energy Agency (ARENA). The data reported in the paper were obtained at the Central Analytical Research Facility (CARF) operated by the Institute for Future Environments at Queensland University of Technology (QUT). Access to CARF was supported by generous funding from the Faculty of Engineering at QUT.

## References

- [1] A. de la Calle, A. Bayon, and J. Pye, "Techno-economic assessment of a high-efficiency, low-cost solar-thermal power system with sodium receiver, phase-change material storage, and supercritical CO<sub>2</sub> recompression Brayton cycle," *Solar Energy*, vol. 199, pp. 885-900, 2020.
- [2] M. Sarvghad, S. Delkassar Maher, D. Collard, M. Tassan, G. Will, and T. A. Steinberg, "Materials compatibility for the next generation of Concentrated Solar Power plants," *Energy Storage Materials*, vol. 14, pp. 179-198, 2018.
- [3] A. International, "E1820-21 Standard test method for measurement of fracture toughness," ed: ASTM International, 2021.
- [4] M. Turski, P. J. Bouchard, A. Steuwer, and P. J. Withers, "Residual stress driven creep cracking in AISI Type 316 stainless steel," *Acta materialia*, vol. 56, pp. 3598-3612, 2008.
- [5] A. J. Horn, A. H. Sherry, and P. J. Budden, "Size and geometry effects in notched compact tension specimens," *The International journal of pressure vessels and piping*, vol. 154, pp. 29-40, 2017.
- [6] M. Sarvghad, S. Bell, R. Raud, T. A. Steinberg, and G. Will, "Stress assisted oxidative failure of Inconel 601 for thermal energy storage," *Solar Energy Materials and Solar Cells*, vol. 159, pp. 510-517, 2017/01/01/ 2017.
- [7] S. Bell, M. Jones, E. Graham, D. Peterson, G. van Riessen, G. Hinsley, et al., "Corrosion mechanism of SS316L exposed to NaCl/Na<sub>2</sub>CO<sub>3</sub> molten salt in air and argon environments," *Corrosion Science*, vol. 195, p. 109966, 2022.
- [8] S. Bell, G. Will, and T. Steinberg, "Corrosion testing under inert atmosphere with stainless steel crucibles," in *AIP Conference Proceedings*, 2019, p. 200004.
- [9] A. Palacios, M. E. Navarro, Z. Jiang, A. Avila, G. Qiao, E. Mura, et al., "High-temperature corrosion behaviour of metal alloys in commercial molten salts," *Solar Energy*, vol. 201, pp. 437-452, 2020/05/01/ 2020.
- [10] Y. Huang, "Oxidation and hot corrosion of metals and alloys," in *Materials corrosion and protection*, ed Berlin: De Gruyter, 2018, pp. 109-178.
- [11] X. Huang, K. Xiao, X. Fang, Z. Xiong, L. Wei, P. Zhu, et al., "Oxidation behavior of 316L austenitic stainless steel in high temperature air with long-term exposure," *Materials Research Express*, vol. 7, p. 066517, 2020/06/01 2020.
- [12] B. Gleeson, "1.09-Thermodynamics and Theory of External and Internal Oxidation of Alloys," *Shreir's corrosion*, pp. 182-184, 2010.
- [13] N. Karimi, F. Riffard, F. Rabaste, S. Perrier, R. Cueff, C. Issartel, et al., "Characterization of the oxides formed at 1000 C on the AISI 304 stainless steel by X-ray diffraction and infrared spectroscopy," *Applied Surface Science*, vol. 254, pp. 2292-2299, 2008.

- [14] K. A. Habib, M. S. Damra, J. J. Saura, I. Cervera, and J. Bellés, "Breakdown and Evolution of the Protective Oxide Scales of AISI 304 and AISI 316 Stainless Steels under High-Temperature Oxidation," *International Journal of Corrosion*, vol. 2011, p. 824676, 2011/08/16 2011.
- [15] M. Zhu, S. Zeng, H. Zhang, J. Li, and B. Cao, "Electrochemical study on the corrosion behaviors of 316 SS in HITEC molten salt at different temperatures," *Solar Energy Materials and Solar Cells*, vol. 186, pp. 200-207, 2018/11/01/ 2018.
- [16] S. Caines, F. Khan, and J. Shirokoff, "Analysis of pitting corrosion on steel under insulation in marine environments," *Journal of Loss Prevention in the Process Industries*, vol. 26, pp. 1466-1483, 2013/11/01/ 2013.
- [17] J. Nguejio, J. Crépin, C. Duhamel, F. Gaslain, C. Guerre, F. Jomard, et al., "Diffusion processes as possible mechanisms for Cr depletion at SCC crack tip," in *Proceedings of the 18th International Conference on Environmental Degradation of Materials in Nuclear Power Systems–Water Reactors*, 2019, pp. 337-357.
- [18] Y. Xu, Y. Gu, W. Zhang, Y. Shi, and K. K. Volodymyr, "Stress-assisted corrosion behaviour of GH3535 alloy in FLiNaK molten salt environment," 2022.
- [19] A. Fattah-alhosseini, A. Saatchi, M. A. Golozar, and K. Raeissi, "The transpassive dissolution mechanism of 316L stainless steel," *Electrochimica acta*, vol. 54, pp. 3645-3650, 2009.
- [20] J. D. Henderson, X. Li, D. W. Shoesmith, J. J. Noël, and K. Ogle, "Molybdenum surface enrichment and release during transpassive dissolution of Ni-based alloys," *Corrosion Science*, vol. 147, pp. 32-40, 2019.
- [21] K. Lakkam, S. M. Kerur, and A. Shirahatti, "Effect of pitting corrosion on the mechanical properties of 316 grade stainless steel," *Materials Today: Proceedings*, vol. 27, pp. 497-502, 2020/01/01/ 2020.
- [22] T. Voisin, R. Shi, Y. Zhu, Z. Qi, M. Wu, S. Sen-Britain, et al., "Pitting corrosion in 316L stainless steel fabricated by laser powder bed fusion additive manufacturing: a review and perspective," *JOM*, pp. 1-22, 2022.